

# Magnetic-Transition-Induced Colossal Magnetoresistance in the Ferrimagnetic Semiconductor $\text{Mn}_3\text{Si}_2\text{Te}_6$

Yiyue Zhang,<sup>1,\*</sup> ZeYu Li,<sup>1,\*</sup> Kunya Yang,<sup>1,\*</sup> Linlin Wei,<sup>1,\*</sup> Xinrun Mi,<sup>1</sup> Aifeng Wang,<sup>1</sup> Xiaoyuan Zhou,<sup>1</sup> Xiaolong Yang,<sup>1,†</sup> Yisheng Chai,<sup>1,‡</sup> and Mingquan He<sup>1,§</sup>

<sup>1</sup>Low Temperature Physics Laboratory, College of Physics & Center of Quantum Materials and Devices, Chongqing University, Chongqing 401331, China

(Dated: December 3, 2024)

In the ferrimagnetic semiconductor  $\text{Mn}_3\text{Si}_2\text{Te}_6$ , a colossal magnetoresistance (CMR) is observed only when a magnetic field is applied along the magnetic hard axis ( $\mathbf{H} \parallel c$ ). This phenomenon suggests an unconventional CMR mechanism potentially driven by the interplay between magnetism, topological band structure, and/or chiral orbital currents (COC). By comparing electrical resistance measurements using continuous direct currents and pulse currents, we found that the current-induced insulator-metal transition, supporting the COC-driven CMR mechanism, is likely a consequence of Joule heating effects. Additionally, multiple magnetic field-induced metamagnetic transitions were identified through AC magnetostriction coefficient experiments, but only when  $\mathbf{H} \parallel c$ . Importantly, the transition at  $\sim 5$  T marks the boundary between the low-field CMR and high-field weak MR. These findings suggest that field-induced metamagnetic transition combined with partial polarization of magnetic moments are the primary causes of the band gap closure, leading to the observed CMR in  $\text{Mn}_3\text{Si}_2\text{Te}_6$ .

The interplay between charge, spin, and lattice degrees of freedom in magnetic systems can give rise to phenomena like giant and colossal magnetoresistance (GMR and CMR). CMR, observed in materials such as  $\text{La}_{1-x}\text{Ca}_x\text{MnO}_3$  [1, 2] and  $\text{Tl}_2\text{Mn}_2\text{O}_7$  [3–5], is characterized by large resistance changes—up to several orders of magnitude—under a magnetic field. This property makes CMR materials promising for high-density storage applications. In doped manganites like  $\text{La}_{1-x}\text{Ca}_x\text{MnO}_3$ , CMR arises from complex mechanisms such as double-exchange interactions, Jahn-Teller distortions, and charge/orbital ordering [6–8]. In  $\text{Tl}_2\text{Mn}_2\text{O}_7$ , CMR is thought to result from interactions between conduction electrons and spin fluctuations or magnetic polarons [3–5]. A common feature of CMR materials is that aligning magnetic moments under a field reduces electron scattering or band gaps, leading to lower electrical resistance.

Recent studies have revealed unique colossal magnetoresistance (CMR) characteristics in the ferrimagnetic semiconductor  $\text{Mn}_3\text{Si}_2\text{Te}_6$ , differing from conventional behavior. As shown in Fig. 1(a),  $\text{Mn}_3\text{Si}_2\text{Te}_6$  adopts a trigonal  $P\bar{3}1c$  structure, where edge-sharing  $\text{MnTe}_6$  octahedra form alternating honeycomb (Mn1) and triangular (Mn2) layers along the  $c$ -axis [9–12]. Below the ferrimagnetic transition temperature ( $T_c \sim 78$  K), magnetic moments on both Mn1 and Mn2 sites order ferromagnetically, primarily within the  $ab$ -plane. Antiferromagnetic coupling between the sublattices results in a ferrimagnetic state. Notably, a drastic negative CMR, up to nine orders of magnitude, occurs only when the magnetic field is applied along the hard  $c$ -axis, contrasting sharply with the moderate negative MR seen when the field is applied in the easy  $ab$ -plane. This highlights a significant departure from typical CMR materials [13–16].

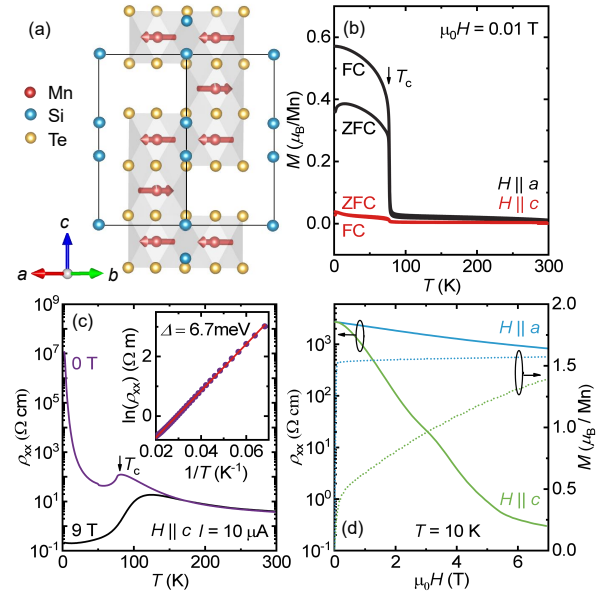


FIG. 1. (a) Side view of the crystal structure of  $\text{Mn}_3\text{Si}_2\text{Te}_6$ , with Mn moments (red arrows) tilted about  $10^\circ$  from the  $ab$ -plane below  $T_c = 78$  K. (b) Temperature-dependent magnetization measured in 0.01 T using zero-field-cooled (ZFC) and field-cooled (FC) protocols for magnetic fields along the  $a$ - and  $c$ -axes. (c) Temperature dependence of resistivity ( $\rho_{xx}$ ) in 0 and 9 T ( $H \parallel c$ ) with a small current ( $I = 10 \mu\text{A}$ ) applied along the  $a$ -axis. Inset: Linear scaling of  $\ln(\rho_{xx})$  versus  $1/T$  between 15 K and 50 K. (d) Comparison of magnetization and resistivity at 10 K for magnetic fields applied along different directions.

Two main scenarios have been proposed to explain the unconventional CMR observed in  $\text{Mn}_3\text{Si}_2\text{Te}_6$ . The first suggests that CMR arises from the reduction of the band gap due to the lifting of spin orientation-dependent nodal-line band degeneracy [15, 17, 18]. In this scenario, when the spins lie within the  $ab$ -plane ( $M \parallel a$ ), a finite band gap exists, and the spin-polarized Te valence bands exhibit a twofold nodal-

\* These authors contributed equally to this work.

† yangxl@cqu.edu.cn

‡ yschai@cqu.edu.cn

§ mingquan.he@cqu.edu.cn

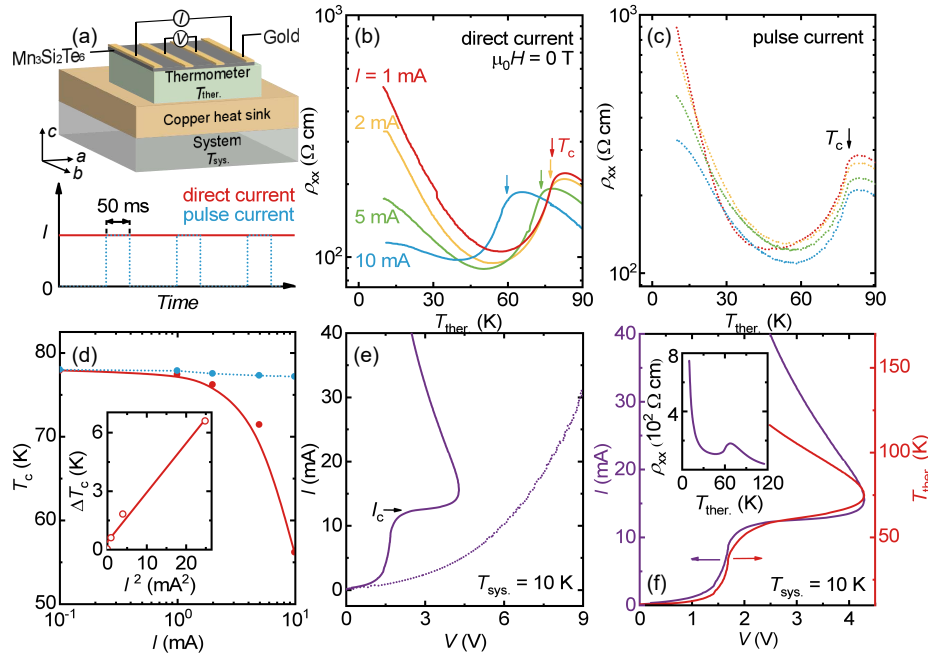


FIG. 2. (a) Upper panel: Schematic of the electrical transport setup, with a  $\text{Mn}_3\text{Si}_2\text{Te}_6$  sample attached to a thermometer and heat sink. Lower panel: Illustration of pulse (blue dashed) and direct (red solid) current modes. (b) and (c): Temperature-dependent resistivity for selected current amplitudes in direct and pulse modes. (d) Current dependence of  $T_c$  for pulse and direct current protocols. Inset: Linear fit of  $\Delta T_c$  vs  $I^2$ . (e) Comparison of  $I - V$  curves at  $T_{\text{sys.}} = 10$  K for direct (solid purple) and pulse (dashed purple) currents. (f) Comparison of  $I - V$  curve with voltage-dependent  $T_{\text{ther.}}$  at  $T_{\text{sys.}} = 10$  K in direct mode. Inset: Resistivity obtained from  $I - V$  data plotted as a function of  $T_{\text{ther.}}$ .

line degeneracy near the Fermi energy. The band gap closes when the spins align along the  $c$ -axis ( $M \parallel c$ ), driving an insulator-to-metal transition and negative CMR [15, 17, 18]. An alternative explanation involves electron scattering due to COC-induced orbital magnetic moments ( $M_{\text{COC}}$ ) [14, 19–21]. In this model,  $M_{\text{COC}}$ , which orients along the  $c$ -axis, is induced by chiral orbital currents running along the Te-Te edges in the  $ab$ -plane of  $\text{MnTe}_6$  octahedra. When a magnetic field is applied along the  $c$ -axis, it aligns these randomly distributed  $M_{\text{COC}}$  domains, reducing electron scattering and lowering resistance. Despite these proposals, the exact mechanism behind the unconventional CMR in  $\text{Mn}_3\text{Si}_2\text{Te}_6$  remains to be fully clarified.

The COC-driven CMR mechanism is supported by electric current tunable properties including current-induced suppression of resistivity and  $T_c$ , and a first-order-like transition in the current-voltage ( $I$ - $V$ ) characteristics [14, 19, 20]. However, Joule heating effects may also contribute to these unusual transport behaviors, especially considering the large resistance ( $\sim 10^3 \Omega$  at 10 K) of typical  $\text{Mn}_3\text{Si}_2\text{Te}_6$  samples (dimensions:  $1 \times 0.5 \times 0.1 \text{ mm}^3$ ) and the large currents (on the order of mA) needed to induce current control of the COC state. To investigate the Joule heating effects, we attached a thermometer directly to the sample and compared the electrical transport behavior under continuous direct and pulse currents. Our results suggest that Joule heating effects likely contribute to the observed current control of electric and magnetic properties. However, the CMR is more strongly associated with magnetic field-induced transitions, which we clearly identify

using a highly sensitive AC magnetostriction coefficient technique. Detailed experimental methods are provided in the Supplemental Materials [22].

Figure 1(b) shows the temperature-dependent magnetization of a  $\text{Mn}_3\text{Si}_2\text{Te}_6$  single crystal, with a ferrimagnetic transition at  $T_c = 78$  K, consistent with previous reports [11–13, 15, 23–26]. In the ferrimagnetic state, the in-plane magnetization ( $H \parallel a$ ) is much larger than the out-of-plane magnetization ( $H \parallel c$ ), indicating an in-plane easy axis [11]. Figure 1(c) shows the temperature-dependent resistivity ( $\rho_{xx}$ ) of a  $\text{Mn}_3\text{Si}_2\text{Te}_6$  sample with a current applied along the  $a$ -axis ( $I \parallel a$ ). In zero magnetic field,  $\rho_{xx}$  shows semiconducting behavior, with a sharp drop below  $T_c$ , likely due to the suppression of spin fluctuations as the material transitions to long-range ferrimagnetism [13, 15, 23, 24]. Fitting the resistivity data between 15 and 50 K with a thermally activated model  $\rho_{xx}(T) = \rho_0 \exp(\Delta/k_B T)$  yields an energy gap of  $\Delta = 6.7(3)$  meV, in agreement with earlier studies [11, 15, 17, 23]. This gap is smaller than the  $\sim 130$  meV gap calculated for Mn moments tilted  $10^\circ$  from the  $ab$ -plane [see Fig. 4], suggesting the presence of impurity bands in real  $\text{Mn}_3\text{Si}_2\text{Te}_6$  samples [15]. When a magnetic field is applied along the  $c$ -axis, the resistivity decreases significantly, with CMR reaching  $\sim 10^8$  at 2 K in 9 T. The negative magnetoresistance extends up to about 150 K, likely due to field-induced suppression of spin fluctuations in the paramagnetic phase [13]. These results indicate that the MR behavior in  $\text{Mn}_3\text{Si}_2\text{Te}_6$  is closely linked to spin degrees of freedom.

Figure 1(d) compares the magnetization and magnetore-

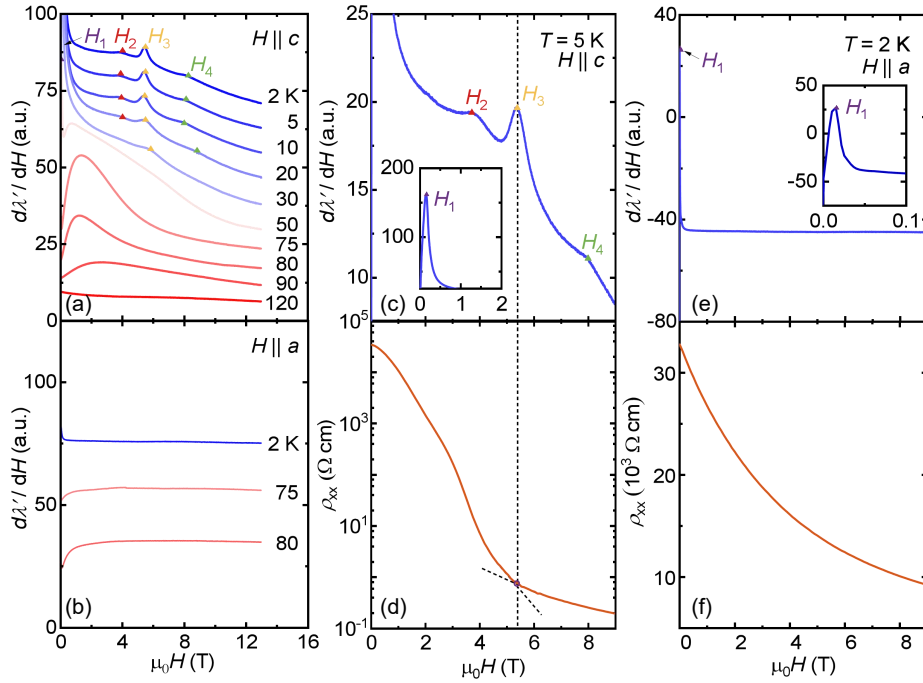


FIG. 3. (a) and (b) Magnetostriction coefficient  $d\lambda'/dH$  vs. magnetic field for  $H \parallel a$  and  $H \parallel c$ . Curves have been vertically shifted for clarity. For  $H \parallel c$ , additional transitions at  $H_2$ ,  $H_3$ , and  $H_4$  appear below 50 K. (d-f) Comparison of magnetostriction with magnetoresistance. The transition at  $H_3$  for  $H \parallel c$  marks the boundary between low-field CMR and high-field moderate MR.

sistance (MR) measured at 10 K with magnetic fields applied along different directions. For  $H \parallel a$ , the magnetization  $M_a$  saturates at  $\sim 1.6 \mu_B/\text{Mn}$  in a small field of  $\sim 0.1$  T. In contrast, for  $H \parallel c$ , saturation is not reached even in 7 T, and magnetic fields above 13 T are required for  $M_c$  to reach  $1.6 \mu_B/\text{Mn}$  [13, 15]. The sharp rise in  $M_c$  below 1 T results from the alignment of magnetic domains [11, 27]. Notably, CMR is observed only when the magnetic field is applied along the magnetic hard  $c$ -axis. In contrast, only moderate negative MR is observed when the field is applied within the easy  $ab$ -plane. Furthermore, within the field range ( $\sim 5$  T) where CMR occurs, the magnetic moment is far from saturation, distinguishing the CMR behavior in  $\text{Mn}_3\text{Si}_2\text{Te}_6$  from other CMR materials where magnetic polarization is essential.

Figure 2 explores the possible origin of current control over the electrical properties of  $\text{Mn}_3\text{Si}_2\text{Te}_6$ . In typical commercial cryostats, such as the Physical Property Measurement System (PPMS), the thermometer is often placed away from the sample, leading to uncertainties in the sample temperature, especially at low temperatures and with large electric currents. To approximate the sample temperature ( $T_{\text{sample}}$ ), the  $\text{Mn}_3\text{Si}_2\text{Te}_6$  sample was directly attached to a thermometer ( $T_{\text{ther}}$ ), which was thermally anchored to a heat sink (a large copper block) [Fig. 2(a)]. However, due to the low thermal conductivity of  $\text{Mn}_3\text{Si}_2\text{Te}_6$  [24], a finite temperature gradient can cause  $T_{\text{sample}}$  to be significantly higher than  $T_{\text{ther}}$  when Joule heating is significant. To minimize contact resistance, a thin layer of gold was sputtered onto the sample before attaching silver epoxy to the current and voltage leads. Additionally, a pulse current protocol (duration: 0.5 ms) was employed, which is shorter

than the thermal relaxation time of the system. This limits the temperature rise of the sample, as the heat capacity of the setup, including the heat sink, is large. For comparison, a continuous direct current (DC) mode, which maintains a constant current, was also used.

In DC mode, both  $T_c$  and resistivity (especially at low temperatures) are significantly suppressed with increasing current [Fig. 2(b)], consistent with previous reports attributing this effect to the COC state [14, 19, 20]. In contrast, in pulse current mode,  $T_c$  and resistivity remain weakly affected by increasing current [Fig. 2(c)]. The difference between DC and pulse current behaviors is highlighted in Fig. 2(d). Notably, the reduction in  $T_c$  induced by DC ( $\Delta T_c = T_c(0) - T_c(I)$ ) scales linearly with  $I^2$  [inset in Fig. 2(d)]. This suggests that  $\Delta T_c$  is proportional to the heat power generated by the DC current, and the observed 'reduction' in  $T_c$  results from inaccurate temperature approximation due to Joule heating. These findings indicate that Joule heating plays a significant role in the current-tunable electrical and magnetic properties of  $\text{Mn}_3\text{Si}_2\text{Te}_6$  under DC.

Distinct  $I - V$  characteristics are observed in DC and pulse current modes [Fig. 2(e)]. In DC mode, an unusual first-order-like transition is seen at a 'critical current'  $I_c \sim 10$  mA, similar to previous studies [14, 19], while a typical semiconductor-like  $I - V$  behavior is observed in pulse mode. In DC mode,  $T_{\text{ther}}$  rises significantly due to Joule heating [Fig. 2(f)]. Notably, the anomalous  $I - V$  curve follows the  $T_{\text{ther}} - V$  curve. When the resistance obtained from the  $I - V$  curve ( $R = V/I$ ) is plotted against  $T_{\text{ther}}$ , the temperature-dependent resistance of  $\text{Mn}_3\text{Si}_2\text{Te}_6$  is recovered, although the inferred ' $T_c$ ' from  $T_{\text{ther}}$  is

lower than the intrinsic  $T_c$ . Similar effects are observed under finite magnetic fields ( $H \parallel c$ ) [see Supplemental Material [22]]. These results suggest that the rapid rise in voltage near  $I_c$  in DC mode is caused by Joule heating, which pushes the sample across  $T_c$ , causing a rapid increase in resistance. In pulse mode,  $T_{\text{ther}}$  increases only slightly, and normal  $I - V$  behavior is observed.

To further investigate the origin of the unusual CMR in  $\text{Mn}_3\text{Si}_2\text{Te}_6$ , we present the ac magnetostriction coefficient ( $d\lambda/dH = d\lambda'/dH + id\lambda''/dH$ ) results in Fig. 3, focusing on the real part ( $d\lambda'/dH$ ). The contrasting behaviors of  $d\lambda'/dH$  for  $H \parallel a$  and  $H \parallel c$  are clearly seen in Figs. 3(a,b). For both configurations and below  $T_c$ ,  $d\lambda'/dH$  rises sharply in weak magnetic fields and peaks around  $H_1$  due to the field-induced alignment of the magnetic domains [see also Fig. 1(d)] [11, 27]. In the vicinity of  $T_c$ , a broad hump appears in  $d\lambda'/dH$  in moderate magnetic fields around 2 T due to the development of spin fluctuations. Well below  $T_c$ ,  $d\lambda'/dH$  is independent of magnetic field with  $H \parallel a$  and above  $H_1$  in the single domain state. On the other hand, for  $H \parallel c$  above  $H_1$ ,  $d\lambda'/dH$  varies continuously with magnetic field due to the continuous rotation of magnetic moments towards the  $c$ -axis [27]. Moreover, a broad peak shows up below 50 K in  $d\lambda'/dH$  at  $H_3 \sim 5$  T and becomes more evident below 20 K accompanied by two more peaks locating at  $H_2 \sim 4$  T and  $H_4 \sim 8$  T. These peak features point to additional field-induced metamagnetic transitions, which are invisible in magnetization measurements. The peak amplitudes of  $d\lambda'/dH$  at  $H_2, H_3, H_4$  are one orders of magnitude smaller compared to that of  $H_1$ . The superior sensitivity of the ac magnetostriction coefficient measurements enables the identification of magnetic transitions that are hard to be resolved by other techniques. Notably, the most significant CMR for  $H \parallel c$  occurs below  $H_3$ , with the MR substantially reduced above this field [see Figs. 3(c,d)]. In contrast, no such metamagnetic transitions are observed for  $H \parallel a$ , which shows weak MR [Figs. 3(e,f)]. These results suggest a strong correlation between the metamagnetic transitions at  $H_3$  and the observed CMR in  $\text{Mn}_3\text{Si}_2\text{Te}_6$ .

In Fig. 4, we summarize the phase diagrams derived from the ac magnetostriction and MR experiments. For  $H \parallel a$ , the phase diagram is relatively simple, showing only the ferrimagnetic transition at  $T_c$  and a field-induced domain re-population at  $H_1$ . In contrast, the phase diagram for  $H \parallel c$  is more complex. In addition to features at  $T_c$  and  $H_1$ , three field-induced metamagnetic transitions are observed at  $H_2, H_3$ , and  $H_4$  below 40 K. Notably, the transition at  $H_3$  marks the boundary between the low-field CMR and high-field weak MR regions. Unlike the sharp CMR observed in perovskite manganites like  $\text{Sm}_{0.5}\text{Ca}_{0.25}\text{Sr}_{0.25}\text{MnO}_3$  [28], the CMR in  $\text{Mn}_3\text{Si}_2\text{Te}_6$  occurs over a broad field range below  $H_3 \sim 5$  T. Therefore, the CMR in  $\text{Mn}_3\text{Si}_2\text{Te}_6$  is not triggered by the metamagnetic transition at  $H_3$ , but is instead associated with continuous changes in physical properties—such as spin fluctuations, COC domains, and band gap—within the magnetic phase below  $H_3$ .

The COC-driven CMR in  $\text{Mn}_3\text{Si}_2\text{Te}_6$  is indirectly supported by the current control of electrical and magnetic properties [14, 19]. As discussed earlier in Fig. 2, Joule heating effects are significant when large currents are applied to the semicon-

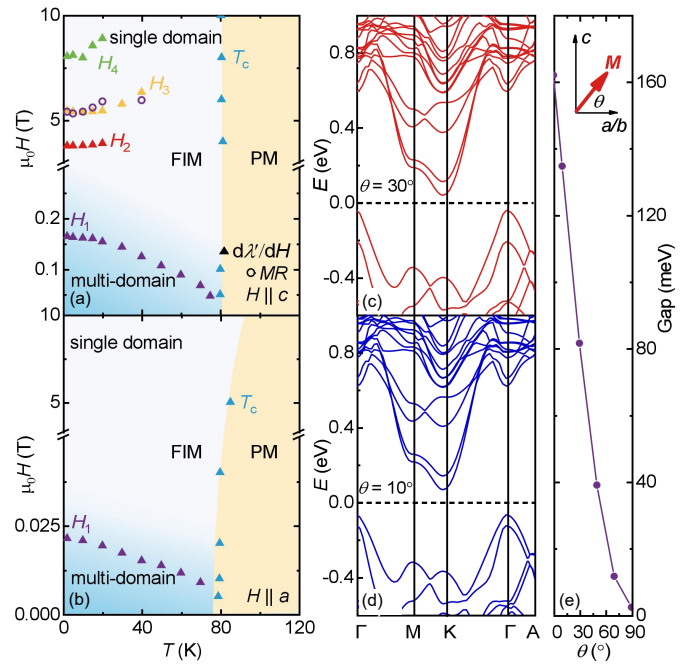


FIG. 4. (a) and (b)  $H - T$  phase diagrams from magnetostriction (filled symbols) and magnetoresistance (open symbols) for  $H \parallel a$  and  $H \parallel c$ . Below  $T_c \sim 78$  K,  $\text{Mn}_3\text{Si}_2\text{Te}_6$  transitions from paramagnetic (PM) to ferrimagnetic (FIM) phase. For  $H \parallel a$ , only one transition occurs at  $H_1$ , while for  $H \parallel c$ , three additional metamagnetic transitions are observed, with  $H_3$  marking the boundary between low-field CMR and high-field moderate MR. (c) and (d) Calculated band structures for  $\theta = 30^\circ$  and  $\theta = 10^\circ$ . (e) Angle dependence of the calculated band gap, with  $\theta$  illustrated in the inset.

ducting  $\text{Mn}_3\text{Si}_2\text{Te}_6$ , particularly at low temperatures. Direct evidence of the COC state remains to be explored. Note that near  $T_c$ , resistivity scales with the magnetic correlation length ( $\xi$ ) as  $\rho \sim \xi^2$ , highlighting the strong interplay between spin fluctuations and electrical transport in  $\text{Mn}_3\text{Si}_2\text{Te}_6$  [27]. The persistence of negative MR above  $T_c$  further underscores the role of spin fluctuations in the magnetotransport properties. Although magnetic fluctuations typically influence transport near  $T_c$  [29, 30], the ferromagnetic-like fluctuations probed by  $d\lambda'/dH$  for  $H \parallel c$  persist well within the ferrimagnetic phase and are continuously suppressed with increasing magnetic field [see Fig. S4 in Supplemental Materials [22]]. However, above  $H_3$ ,  $d\lambda'/dH$  continues to decrease with a slope similar to that below  $H_3$ , indicating that coupling between conducting electrons and spin fluctuations alone cannot fully explain the CMR observed below  $H_3$ . Furthermore, pressure-induced volume compression of  $\sim 7\%$  can also induce an insulator-metal transition in  $\text{Mn}_3\text{Si}_2\text{Te}_6$  [18], though the field-induced magnetostriction at ambient pressure is only on the order of a few hundred ppm [14], making magnetostriction an unlikely cause of the CMR.

The most probable scenario to explain the CMR in  $\text{Mn}_3\text{Si}_2\text{Te}_6$  is then the field-induced suppression of band gap [15, 17, 18]. Similar spin orientation-dependent band gap has also been proposed to explain the CMR observed in  $\text{EuMnSb}_2$

[31] and  $\text{EuTe}_2$  [32]. Although in  $\text{Mn}_3\text{Si}_2\text{Te}_6$  the magnetic moments only tilt slightly from about  $10^\circ$  in zero field to about  $30^\circ$  towards the  $c$ -axis around  $H_3$  [27], our calculations show that the band gap is reduced by about 50 meV [see Fig. 4(d)], agreeing well with early calculations [17]. This value is larger than the gap size  $\sim 7$  meV of real samples. Moreover, in zero magnetic field,  $\text{Mn}_3\text{Si}_2\text{Te}_6$  favors a noncollinear magnetic state [27]. The field-induced metamagnetic transition at  $H_3$  for  $H \parallel c$  could be the transition from a noncollinear magnetic structure to a collinear magnetic state. The field-tuned suppression of noncollinearity in magnetic structure, together with partial polarization of the magnetic moments along the  $c$ -axis, are sufficient to close the band gap and lead to the CMR. In addition, the topological Nernst effect, which is linked to the noncollinear magnetic structure, also appears within the CMR field range [23], further supporting the connection between the field-tuned magnetic structure and the CMR. The nature of the transition at  $H_3$  warrants further investigation, and we hope that our findings will encourage further studies to explore the relationship between the field-tuned magnetic structure and CMR in  $\text{Mn}_3\text{Si}_2\text{Te}_6$ .

In summary, we have investigated Joule heating effects in

the electric current control of magnetic and electrical transport properties in  $\text{Mn}_3\text{Si}_2\text{Te}_6$ . By comparing results from pulse and direct current modes, we found that Joule heating significantly influences the measurements in direct current mode. The exact nature of the proposed COC state remains unclear. Notably, for  $H \parallel c$ , we observed additional field-induced metamagnetic transitions in magnetostriction experiments, which have not been previously reported. The transition at  $H_3 \sim 5$  T marks the boundary between low-field CMR and high-field moderate MR. These results suggest that the field-tuned magnetic structure plays a crucial role in the CMR behavior of  $\text{Mn}_3\text{Si}_2\text{Te}_6$ .

We thank Quansheng Wu for fruitful discussions. We thank Guiwen Wang and Yan Liu at the Analytical and Testing Center of Chongqing University for technical support. This work has been supported by National Natural Science Foundation of China (Grants Nos. 12474141, 12374038), the Open Fund of the China Spallation Neutron Source Songshan Lake Science City (Grant No. KFKT2023B07), Fundamental Research Funds for the Central Universities, China (Grant No. 2024CDJXY022), Chinesisch-Deutsche Mobilitatsprogramm of Chinesisch-Deutsche Zentrum fur Wissenschaftsforderung (Grant No. M-0496).

- 
- [1] A. P. Ramirez, *J. Phys.: Condens. Matter* **9**, 8171 (1997).  
 [2] Y. Tokura, *Rep. Prog. Phys.* **69**, 797 (2006).  
 [3] Y. Shimakawa, Y. Kubo, and T. Manako, *Nature* **379**, 53 (1996).  
 [4] M. A. Subramanian, B. H. Toby, A. P. Ramirez, W. J. Marshall, A. W. Sleight, and G. H. Kwei, *Science* **273**, 81 (1996).  
 [5] A. P. Ramirez and M. A. Subramanian, *Science* **277**, 546 (1997).  
 [6] C. Zener, *Phys. Rev.* **82**, 403 (1951).  
 [7] P. G. de Gennes, *Phys. Rev.* **118**, 141 (1960).  
 [8] P. W. Anderson and H. Hasegawa, *Phys. Rev.* **100**, 675 (1955).  
 [9] H. Vincent, D. Leroux, D. Bijaoui, R. Rimet, and C. Schlenker, *J. Solid State Chem.* **63**, 349 (1986).  
 [10] R. Rimet, C. Schlenker, and H. Vincent, *J. Magn. Magn. Mater.* **25**, 7 (1981).  
 [11] A. F. May, Y. Liu, S. Calder, D. S. Parker, T. Pandey, E. Cakmak, H. Cao, J. Yan, and M. A. McGuire, *Phys. Rev. B* **95**, 174440 (2017).  
 [12] A. F. May, H. Cao, and S. Calder, *J. Magn. Magn. Mater.* **511**, 166936 (2020).  
 [13] Y. Ni, H. Zhao, Y. Zhang, B. Hu, I. Kimchi, and G. Cao, *Phys. Rev. B* **103**, L161105 (2021).  
 [14] Y. Zhang, Y. Ni, H. Zhao, S. Hakani, F. Ye, L. DeLong, I. Kimchi, and G. Cao, *Nature* **611**, 467 (2022).  
 [15] J. Seo, C. De, H. Ha, J. E. Lee, S. Park, J. Park, Y. Skourski, E. S. Choi, B. Kim, G. Y. Cho, *et al.*, *Nature* **599**, 576 (2021).  
 [16] J. Wang, S. Wang, X. He, Y. Zhou, C. An, M. Zhang, Y. Zhou, Y. Han, X. Chen, J. Zhou, and Z. Yang, *Phys. Rev. B* **106**, 045106 (2022).  
 [17] Y. Zhang, L.-F. Lin, A. Moreo, and E. Dagotto, *Phys. Rev. B* **107**, 054430 (2023).  
 [18] R. A. Susilo, C. I. Kwon, Y. Lee, N. P. Salke, C. De, J. Seo, B. Kang, R. J. Hemley, P. Dalladay-Simpson, Z. Wang, D. Y. Kim, K. Kim, S. W. Cheong, H. W. Yeom, K. H. Kim, and J. S. Kim, *Nat. Commun.* **15**, 3998 (2024).  
 [19] Y. Zhang, Y. Ni, P. Schlottmann, R. Nandkishore, L. E. DeLong, and G. Cao, *Nat. Commun.* **15**, 3579 (2024).  
 [20] Z. Zhang, G. Liu, W. Qi, H. Xie, J. Guo, Y. Du, T. Wang, H. Zhang, F. Zhou, J. Li, Y. Zhang, Y. Yu, F. Fei, X. Xi, and F. Song, *AIP Advances* **14**, 035238 (2024).  
 [21] S. W. Lovesey, *Phys. Rev. B* **107**, 224410 (2023).  
 [22] See supplemental material for experimental and calculation methods, and more detailed data.  
 [23] C. Ran, X. Mi, J. Shen, H. Wang, K. Yang, Y. Liu, G. Wang, G. Wang, Y. Shi, A. Wang, Y. Chai, X. Yang, M. He, X. Tong, and X. Zhou, *Phys. Rev. B* **108**, 125103 (2023).  
 [24] Y. Liu, Z. Hu, M. Abeykoon, E. Stavitski, K. Attenkofer, E. D. Bauer, and C. Petrovic, *Phys. Rev. B* **103**, 245122 (2021).  
 [25] Y. Liu and C. Petrovic, *Phys. Rev. B* **98**, 064423 (2018).  
 [26] C. Bigi, L. Qiao, C. Liu, P. Barone, M. C. Hatnean, G.-R. Siemann, B. Achinuq, D. A. Mayoh, G. Vinai, V. Polewczyk, D. Dagur, F. Mazzola, P. Bencok, T. Hesjedal, G. van der Laan, W. Ren, G. Balakrishnan, S. Picozzi, and P. D. C. King, *Phys. Rev. B* **108**, 054419 (2023).  
 [27] F. Ye, M. Matsuda, Z. Morgan, T. Sherline, Y. Ni, H. Zhao, and G. Cao, *Phys. Rev. B* **106**, L180402 (2022).  
 [28] S. Banik, K. Das, T. Paramanik, N. P. Lalla, B. Satpati, K. Pradhan, and I. Das, *NPG Asia Mater.* **10**, 923 (2018).  
 [29] P. Majumdar and P. B. Littlewood, *Nature* **395**, 479 (1998).  
 [30] P. Majumdar and P. Littlewood, *Phys. Rev. Lett.* **81**, 1314 (1998).  
 [31] Z. L. Sun, A. F. Wang, H. M. Mu, H. H. Wang, Z. F. Wang, T. Wu, Z. Y. Wang, X. Y. Zhou, and X. H. Chen, *npj Quantum Mater.* **6**, 94 (2021).  
 [32] J. Yin, C. Wu, L. Li, J. Yu, H. Sun, B. Shen, B. A. Frandsen, D.-X. Yao, and M. Wang, *Phys. Rev. Mater.* **4**, 013405 (2020).